Journal of Medicinal Chemistry

pubs.acs.org/jmc

Article

Computational Design of Potent D-Peptide Inhibitors of SARS-CoV-2

Pedro A. Valiente, Han Wen, Satra Nim, JinAh Lee, Hyeon Ju Kim, Jinhee Kim, Albert Perez-Riba, Yagya Prasad Paudel, Insu Hwang, Kyun-Do Kim, Seungtaek Kim, and Philip M. Kim*

Cite This: https://doi.org/10.1021/acs.jmedchem.1c00655

Read Online

ACCESS | Metrics & More | Article Recommendations | Supporting Information

ABSTRACT: Blocking the association between the severe acute respiratory syndrome coronavirus 2 (SARS-CoV-2) spike protein receptor-binding domain (RBD) and the human angiotensin-converting enzyme 2 (ACE2) is an attractive therapeutic approach to prevent the virus from entering human cells. While antibodies and other modalities have been developed to this end, D-amino acid peptides offer unique advantages, including serum stability, low immunogenicity, and low cost of production. Here, we designed potent novel D-peptide inhibitors that mimic the ACE2 α1-binding helix by searching a mirror-image version of the PDB. The two best designs bound the RBD with affinities of 29 and 31 nM and blocked the infection of Vero cells by SARS-CoV-2 with IC_{50} values of 5.76 and 6.56 μM, respectively. Notably, both D-peptides neutralized with a similar potency the infection of two variants of concern: B.1.1.7 and B.1.351 *in vitro*. These potent D-peptide inhibitors are promising lead candidates for developing SARS-CoV-2 prophylactic or therapeutic treatments.

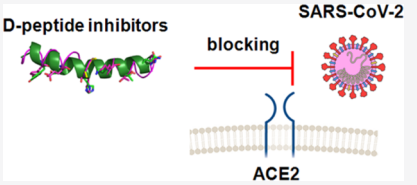

INTRODUCTION

COVID-19 caused by the novel severe acute respiratory syndrome coronavirus 2 (SARS-CoV-2) virus has become a pandemic, causing fever, severe respiratory illness, and pneumonia.[1] In the last two decades, two other coronaviruses, SARS-CoV (2002−2003) and Middle East respiratory syndrome coronavirus (MERS-CoV, 2012-present), have caused global outbreaks. All CoV's encode a surface spike glycoprotein, which binds to the host-cell receptor and mediates viral entry.[2] For betacoronaviruses, a single region of the spike protein called the receptor-binding domain (RBD) mediates the interaction with the host-cell receptor. After binding the receptor, a nearby host protease cleaves the spike, releasing the spike fusion peptide and facilitating virus entry.[3−6] Earlier studies revealed that SARS-CoV-2 uses the human angiotensin-converting enzyme 2 (ACE2) receptor for cell entry, similarly to SARS-CoV.[7−11]

SARS-CoV-2 infection usually initiates in the nasal cavity, where the virus replicates for many days before propagating to the whole respiratory system.[12] The intranasal delivery of high doses of viral inhibitors might thus provide preventive and/or therapeutic benefits for early infection management. This could be beneficial for medical professionals and others who regularly interact with infected people.[13] Numerous neutralizing antibodies targeting the RBD of SARS-CoV-2 are being developed as effective therapies for COVID-19.[14−21] However, antibodies have disadvantages, in particular, for intranasal delivery, due to their large size; moreover, they are very expensive to produce, making them poor candidates for mass therapeutics or for application in developing countries. Also, a set of high-affinity protein minibinders targeting the spike RBD and able to neutralize the SARS-CoV-2 infection *in vitro* were described.[13] However, the proteolytic activity or immune response of the host against these proteins could limit their therapeutic or prophylactic applications.

Scientists around the world have been developing anti-SARS-CoV-2 vaccines in response to the COVID-19 outbreak. Over 300 vaccination initiatives have been developed as a result of an extraordinary effort by the scientific community.[22] Over 78 are now undergoing clinical evaluation, 32 of these are in phase III clinical trials, and 11 of them have completed phase III with positive results.[23] However, the production, distribution, and equity access of billions of doses of COVID-19 vaccines for the entire world population is the new, complex challenge.[22]

Peptides consisting of D-amino acids have unique advantages, including low immunogenicity, low manufacturing cost, and proteolytic stability. Note that a peptide viral entry inhibitor, fuzeon, has been approved for the treatment of HIV,[24] and a D-amino acid analogue of it has been in development.[25] Here, we develop novel D-peptide inhibitors of the RBD−ACE2 interaction using an in-house methodology for converting (L)-peptides to highly stable D-analogues after searching a mirror-image version of the PDB (D-PDB).[26] Two designs bound the RBD with affinities of 29 and 31 nM, respectively. Both D-peptides inhibited the SARS-CoV-2 infection in Vero cells with IC_{50} values of 5.76 and 6.56 μM. Notably, both D-peptides neutralized with a similar potency the infection of two variants of concern: B.1.1.7 and B.1.351.

Received: April 9, 2021

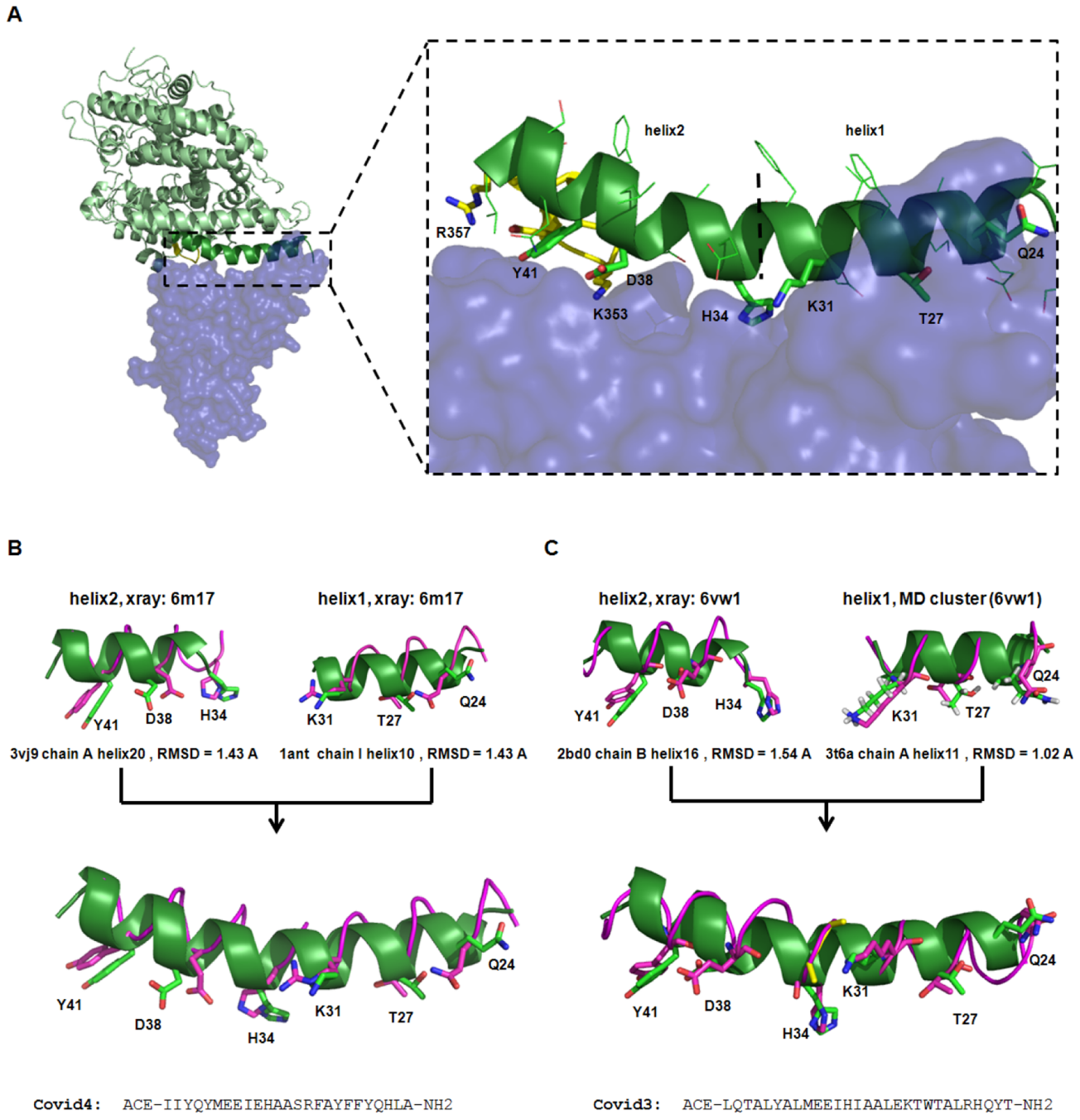

Figure 1. Design strategy of the novel D-peptide binders of the SARS-CoV-2 spike RBD. (A) On the right, the structure of the SARS-CoV-2 RBD (green, cartoon) bound with ACE2 (blue, surface). On the left, a zoom-in image of the ACE2-binding interface with the RBD. In green, the ACE2 N terminus-binding helix. In yellow, the ACE2 hairpin loop L351−R357. To run the query process, the binding helix was split into two fragments: I21−N33 and H34 to L45. For clarity, only the hotspots in the binding helix (Q24, T27, K31, H34, D38, and Y41) and hairpin helix (K353 and R357) were highlighted as licorice. (B) Structural alignment of the best D-matches obtained for the helix1 (6m17) and helix2 (6m17). Structural superposition of full D-peptide (Covid4) over the binding helix extracted from the full-length ACE2 receptor. The hotspot and matching residues in the L- and D-peptides are showed as licorice. (C) Structural alignment of the best D-matches obtained for the helix1 (MD cluster) and helix2 (6vw1). Structural superposition of the full D-peptide (Covid3) over the binding helix extracted from the ACE2 n-terminal peptidase domain. The hotspot and matching residues in the L- and D-peptides are showed as licorice. ACE (acetyl group) and NH_2 (amide group).

These potent D-peptide inhibitors are promising lead candidates for developing SARS-CoV-2 prophylactic or therapeutic treatments.

RESULTS

Design of Novel D-Peptide Binders of the SARS-CoV-2 Spike Protein. Targeting the RBD−ACE2 interaction is a therapeutic or preventive strategy to block the first step of the SARS-CoV-2 infection.[15,17,22,27] Here, we design novel D-peptide binders of the SARS-CoV-2 spike protein based on the ACE2-binding helix by searching a D-PDB database with an in-house methodology able to convert L-peptides to highly stable D-analogues.[26] As the first step in our strategy, we predicted the hotspot residues at the ACE2-binding interface through

https://doi.org/10.1021/acs.jmedchem.1c00655
J. Med. Chem. XXXX, XXX, XXX−XXX

computational alanine scanning (CAS) using the Elaspic2 webserver (http://elaspic.kimlab.org).[28] CAS calculations indicated that residues Q24 ($\Delta\Delta G_{calc}$ = 0.87 kcal/mol), K31 ($\Delta\Delta G_{calc}$ = 1.43 kcal/mol), D38 ($\Delta\Delta G_{calc}$ = 1.01 kcal/mol), Y41 ($\Delta\Delta G_{calc}$ = 2.14 kcal/mol), K353 ($\Delta\Delta G_{calc}$ = 0.83 kcal/mol), D355 ($\Delta\Delta G_{calc}$ = 0.79 kcal/mol), and R357 ($\Delta\Delta G_{calc}$ = 1.26 kcal/mol) were the major contributors of ACE2 to the binding affinity of the RBD−ACE2 complex (Figure S1). A deep mutagenesis study on the ACE2-binding interface supported these predictions.[29] Of relevance, residues Q24, K31, D38, and Y41 are located within the ACE2-binding helix, while positions K353, D355, and R357 are within the hairpin loop (Figure 1A).

We used the ACE2-binding helix extracted from the experimental structures of the RBD in complex with the n-terminal peptidase domain (PDB code: 6vw1) or the full-length human ACE2 (6m17) as a starting point to design novel antispike D-peptide binders. Before querying the D-PDB database, we split the ACE2-binding helix into two fragments that we denoted as helix1 and helix2. Helix1 runs from I21 to N33, while helix2 runs from H34 to L45. In helix1, we defined Q24, T27, and K31 as hotspots. For helix2, we identified H34, D38, and Y41 (Figure 1A) as hotspots. Forty query structures were generated for helix1 and 36 for helix2 by combining different sets of specific atom levels extracted from the hotspot residues (Table SI). After running the query process for each helix independently, several matches were located at the D-PDB database (Table SII). The root-mean-square deviation (rmsd) profiles of the 1000 best output structures in the D-PDB database search for each helix are shown in Figure S2. Match quality was measured through the rmsd between the specific atoms in each query structure and the matched structures at D-PDB (Figure 1B,C). For the full-length ACE2 structure, the best match for helix1 was found in 3vj9 at 1.43 A and in 1ant at 1.43 A for helix2 (Figure 1B). For the protease domain ACE2 structure, the best match for helix2 was found in 2bd0 at 1.54. While no suitable matches with rmsd below 1.6 A were identified for helix1 (Figure 1C) from the crystal structure, we used an alternative strategy. Recently, a 10 μs molecular dynamics (MD) simulation of the human ACE2 structure in complex with the RBD (6vw1) was released by D. E. Shaw Research,[29] and we reasoned that a representative structure from such simulations may actually provide a better template for matching; we thus used the most representative clusters as templates for our match. The best match for helix1 was found in 3t6a at 1.02 A (Figure 1C). Next, we joined the best matches to generate four D-peptides named Covid1, Covid2, Covid3, and Covid4. We added two (DAla−DAla) or three extra residues (DIle−DAla−DAla) to link both helices in each D-peptide because both residues are strong helix stabilizers (Table 1, Figure 1B,C).

We built the 3D structure of the spike + D-peptide complexes by superimposing the D-peptides into the X-ray structure of the RBD−ACE2 complex (6VW1, Figure 2A). Next, we evaluated the stability of the spike + D-peptide complexes through MD simulations of 200 ns. All the MD simulations were set up without adding glycosylations to the RBD structure (segment N331−E516). This domain lacks the two key *N*-glycosylation sites: N165 and N234, in modulating the conformational dynamics of the spike's RBD.[30] We did not model the glycans at positions N331 and N343 because they are too far from the D-peptide-binding site in the RBD (Figure S3). The rmsd profiles calculated along the MD simulations for the peptides' heavy atoms showed Covid3 and Covid4 as the D-peptides with the most stable binding mode (Figure 2B). The root-mean-square fluctuation (RMSF) values below 0.2 nm in most of the residues indicated good stability in the binding mode of both peptides (Figure S4). We also superimposed the initial and final structures obtained from the MD simulations of the complexes RBD + Covid3 and RBD + Covid4. For Covid3, the more significant displacement is observed at the N-terminal (first three residues), while for Covid4, the more notable fluctuations were observed in the N-terminal and C-terminal region of this peptide. Both peptides rapidly stabilize in a new average position close to the initial structure (Figure S5). Thus, we selected these peptides for further experimental validation.

Table 1. Sequences of the Design of Retro-Inverted D-Peptide Binders of the SARS-CoV-2 Spike RBD[b]

D-peptide code	full sequence[a]
Covid1	LEEWYKFIEESIH**AA**LEKTWTALRHQYT
Covid2	ILMDKIYKYAEIIH**AA**LEKTWTALRHQYT
Covid3	LQTALYALMEEIH**IAA**LEKTWTALRHQYT
Covid4	IIYQYMEEIEH**AA**SRFAYFFYQHLA
Covid_extented_1	RFDGKGL**G**IYQYMEEIEH**AA**SRFAYFFYQHLA

[a]The full sequence of each peptide is obtained by combining helix2 + linker + helix1. [b]In bold are highlighted the linker residues to join helix2 and helix1.

A previous computational design study suggested that it might be possible to increase the spike binding affinity of α-helical peptide blockers by grafting the hairpin loop L351−R357 to the peptide structure.[31] To explore how to improve the affinity of the D-peptide analogues Covid3 and Covid4 by adding the retro-inverse (RI) sequence of the hairpin loop, we superposed the most representative structure extracted from the MD simulations of both peptides over the X-ray structure of the RBD−ACE complex (6vw1). The clashes observed between the N-terminal region of Covid3 and the hairpin loop showed that adding the hairpin loop RI sequence to this peptide structure is not suitable (Figure 2C). In the case of Covid4, the structural superposition suggested the chance to extend the N-terminal region of this peptide by adding the RI sequence (Figure 2D). This modification might increase the binding affinity for the spike protein. We named the extended version of Covid4 as Covid_extended_1 (Table 1).

Experimental Validation of the Design of D-Peptides. We performed circular dichroism (CD) measurements and size-exclusion chromatography (SEC) of the peptides in solution to determine the peptides' secondary structure and oligomerization states. These analyses indicate that the D-peptides remain as helical monomers in solution (Figures 3 and S6). Of relevance, the D-peptides showed a higher helical content than the L-peptide (I21−S43) derived from the central helix of the ACE2. Next, we assessed whether Covid3, Covid4, and Covid_extended_1 could directly bind the RBD by performing biolayer interferometry (BLI) experiments. Ni-NTA (nitrilotriacetic acid) biosensors were used to immobilize precisely His-tagged RBD and then test for direct binding of the synthesized peptides. We found that all three peptides could bind the RBD but with different affinities. Kinetic fits show that Covid extended_1 bound to the RBD with the highest affinity (29 ± 0.25 nM), followed by Covid3 (31 ± 0.25 nM), and Covid4 with about threefold lower affinity (105 ± 0.17 nM) (Figure 4A−C). As a positive control, we

https://doi.org/10.1021/acs.jmedchem.1c00655
J. Med. Chem. XXXX, XXX, XXX−XXX

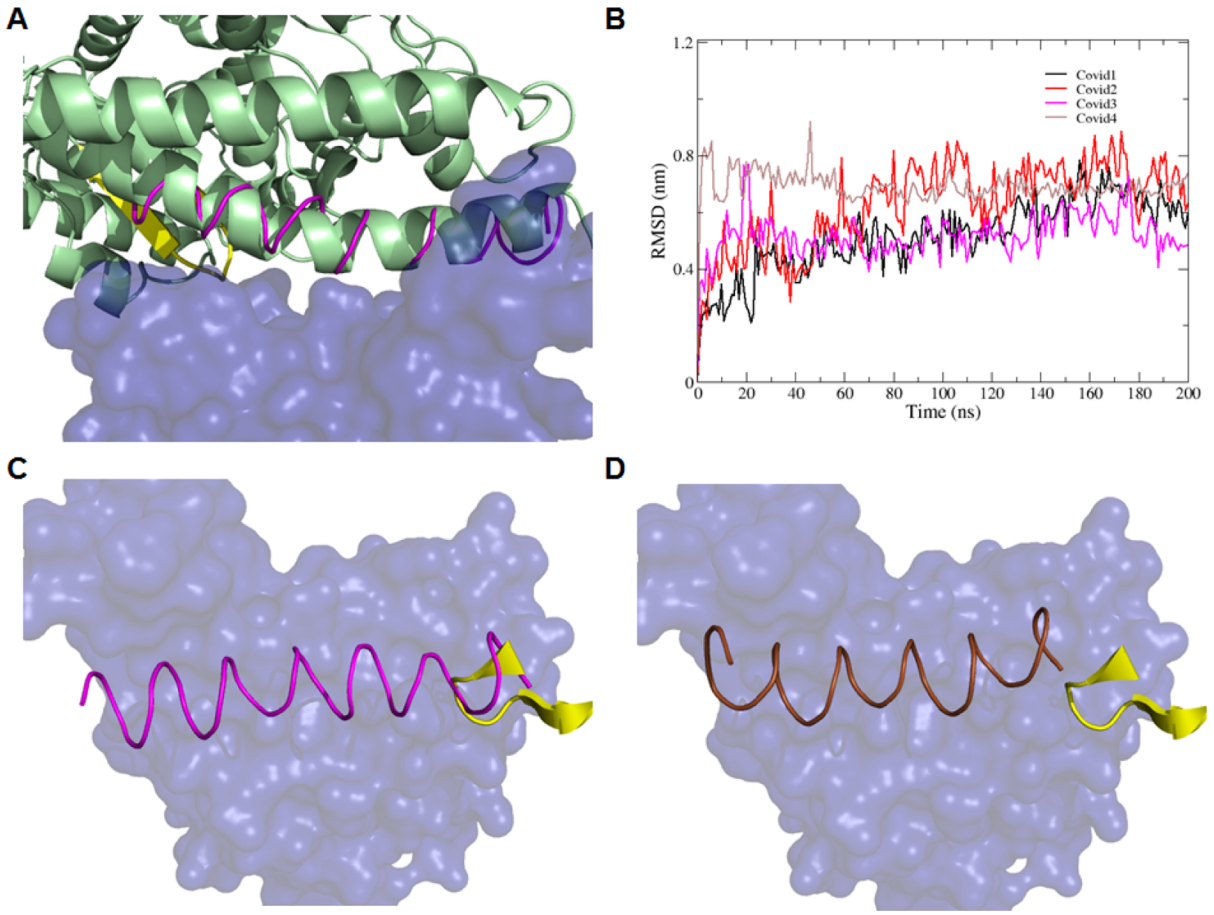

Figure 2. Modeling the 3D structure of the SARS-CoV-2 RBD bound to the D-peptides. (A) Superposition of the 3D structure of D-peptides over the structure of the spike RBD (green, cartoon) bound to the ACE2 receptor (blue, surface). In magenta is shown a representative D-peptide (Covid3). (B) rmsd of the heavy atoms of the design of D-peptides bound to the RBD. (C) Structural superposition of the most representative structure extracted from the MD simulation of Covid3 (magenta, cartoon) bound to the RBD (blue, surface) over the RBD−ACE2 X-ray structure (6vw1). The hairpin loop L351−R357 (yellow) of the ACE2 receptor in the X-ray structure was only represented for clarity. (D) Structural superposition of the most representative structure extracted from the MD simulation of Covid4 (brown, cartoon) bound to the RBD (blue, surface) over the RBD−ACE2 X-ray structure (6vw1). The hairpin loop (yellow) of the ACE2 receptor in the X-ray structure was only represented for clarity. Clashes between Covid3 and the hairpin loop were observed after the structural superposition.

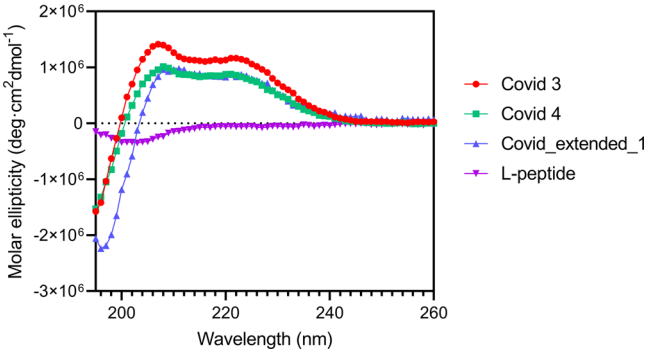

Figure 3. CD measurements of the peptides in solution.

measured the binding affinity of the RBD−ACE2 complex (K_d = 8.8 ± 0.17 nM) (Figure 4D).

The resistance to protease degradation is an attractive property of D-peptides for biomedical applications, as it leads to extended half-life in serum. We carried out a comparative analysis of the resistance to proteinase K (ProtK) degradation of Covid3, Covid_extended_1, and L-peptide derived from the ACE2 N-terminal-binding helix (I21−L45). We observed an 80% loss of the L-peptide in less than 1 h, while 82.88% of Covid3 and 87.45% of Covid_extended_1 can still be detected after 2.5 h exposure to ProtK (Figure 5A,B).

Finally, we investigated the ability of Covid3 and Covid_extended_1 to inhibit the infection of Vero cells by SARS-CoV-2. Both peptides were mixed with 100 fifty-percent tissue-culture-infective dose ($TCID_{50}$) of SARS-CoV-2 before being incubated to Vero cell monolayers at different concentrations. Covid extended_1 and Covid3 blocked SARS-CoV-2 infection with IC_{50}'s of 5.76 ± 2.14 and 6.56 ± 1.65 μM, respectively (Figure 6). We estimated the K_i of both peptides from the IC_{50} values obtained in the virus neutralization assays using the Cheng−Prusoff equation.[32] Of relevance, the K_i values are in the same potency range as observed in the BLI binding assays (Table SIII). We also included a rabbit polyclonal antibody (40150-T62-COV2, Sino Biological Inc., Beijing, China) and the first international standard for anti-SARS-CoV-2 immunoglobulin (NIBSC code 20/136) (Figure S7) as positive controls. The virus neutralization for controls and D-peptides as a function of the dilution ratio is shown in Figure S7. We also evaluated the cytotoxicity of the D-peptides in Vero cells. As can be seen,

https://doi.org/10.1021/acs.jmedchem.1c00655
J. Med. Chem. XXXX, XXX, XXX−XXX

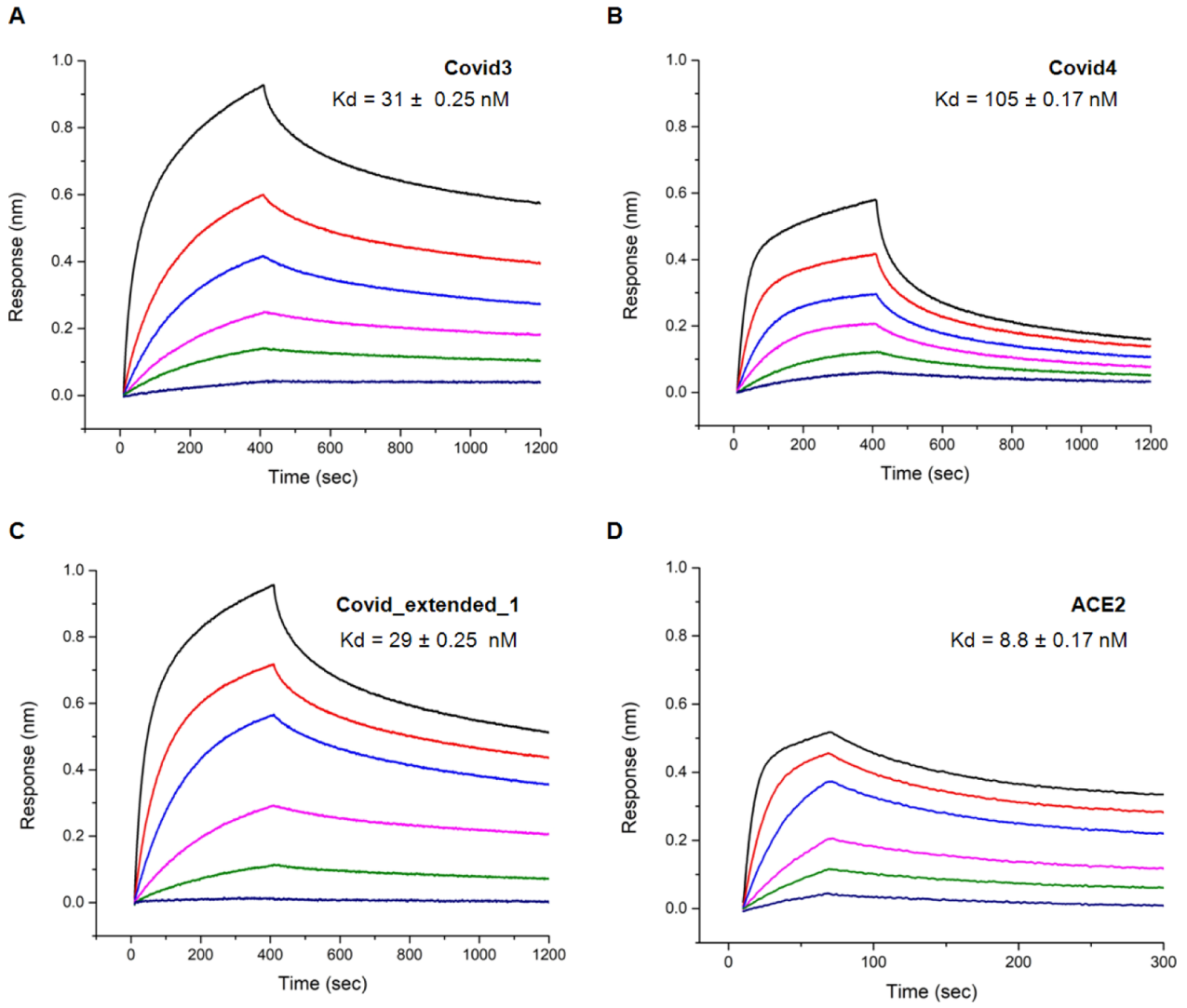

Figure 4. Design of D-peptides bound to the RBD. (A) Binding of Covid3 to the RBD monitored by BLI (K_d = 31 ± 0.25 nM). (B) Binding of Covid4 to the RBD monitored by BLI (K_d = 105 ± 0.17 nM). (C) Binding of Covid_extended_1 to the RBD monitored by BLI (K_d = 29 ± 0.25 nM). (D) Binding of ACE2 to the RBD monitored by BLI (K_d = 8.8 ± 0.17 nM). With different line colors were highlighted the ACE2 concentrations loaded to the sensors: as black (1 μM), red (0.5 μM), blue (0.25 μM), magenta (0.125 μM), green (0.063 μM), and dark blue (0.031 μM).

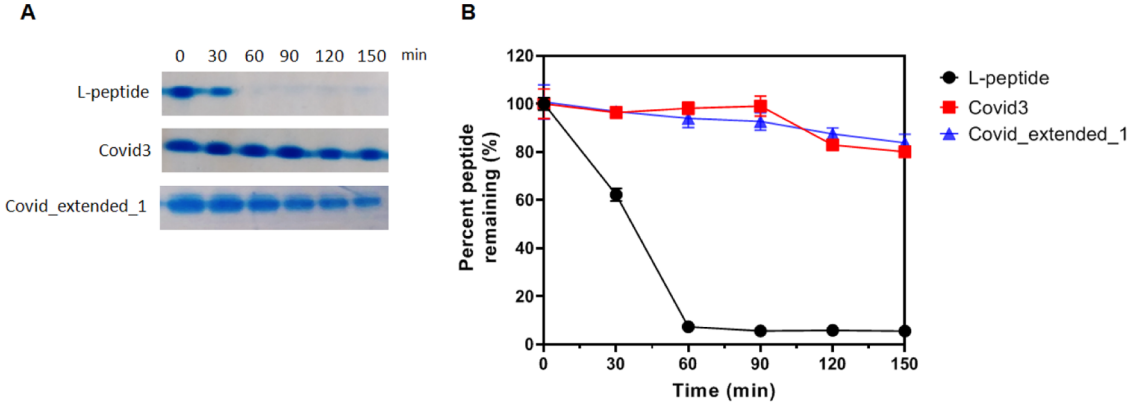

Figure 5. Design of D-peptides are resistant to ProtK degradation. (A) Sample gel images of the L-peptide derived from the ACE2 (I21−L45) and the D-peptides Covid3 and Covid_extended_1 treated with ProtK over 150 min. Gels were stained with Coomassie Brilliant Blue dye. (B) Quantification of remaining peptide post-ProtK treatment in 30 min intervals.

both peptides are not toxic in the range of concentrations tested in the virus neutralization assays (Figure S8).

Design of D-Peptides That Inhibit the Infection of Vero Cells by SARS-CoV-2 Variants B.1.1.7 and B.1.351.

https://doi.org/10.1021/acs.jmedchem.1c00655
J. Med. Chem. XXXX, XXX, XXX−XXX

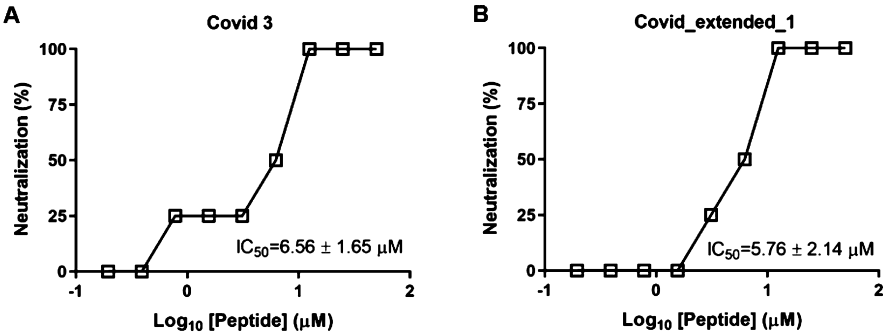

Figure 6. Neutralization of SARS-CoV-2 infection in Vero cells by the design of D-peptide inhibitors. (A) Neutralization activity of Covid3. (B) Neutralization activity of Covid_extended_1. Different concentrations of both peptides were mixed with 100 $TCID_{50}$ of SARS-CoV-2 before being incubated with Vero cell monolayers. Covid3 and Covid_extended_1 blocked SARS-CoV-2 infection with an IC_{50} of 6.56 ± 2.14 and 5.76 ± 1.65 μM, respectively.

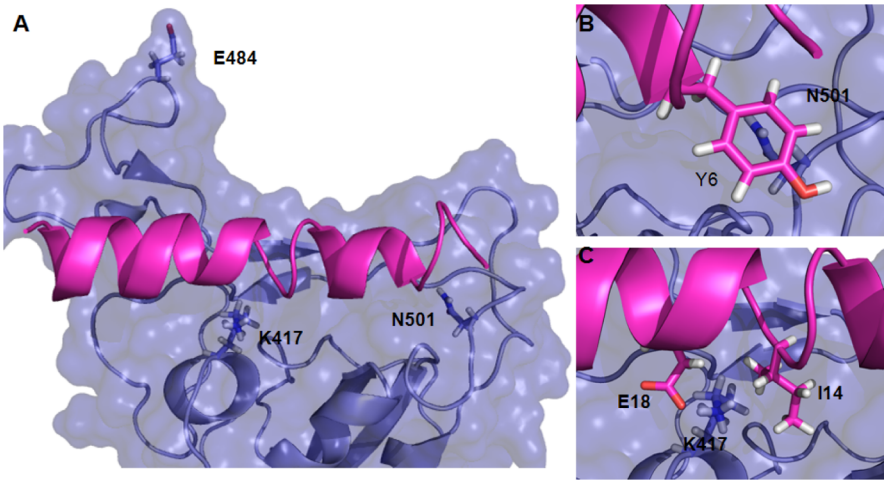

Figure 7. Mapping mutations of the most current circulating isolates of SARS-CoV-2 within the D-peptides' binding interface. (A) Only two positions (N501 and K417) are within the binding interface of Covid3 with the RDB. All the residues within 0.5 nm of the peptide were included in the binding interface. Based on this cutoff, E484 is outside the binding interface. (B) Zoom-in image of the binding contact of the residue N501 with Covid3. Residue Y6 of Covid3 is in close interaction with N501. (C) Zoom-in image of the binding contact of residue K417 with Covid3. Residues I14 and E18 are interacting with K417.

First, we explored *in silico* the ability of our D-peptides to bind the RBD of the most current circulating SARS-CoV-2 isolates reported in the UK (N501Y, A570D, D614G, and P681H), South Africa (K417N, E484K, N501Y, and D614G), Brazil (K417T, E484K, N501Y, and D614G), and Japan (K417N, E484K, N501Y, and D614G). These spike proteins contain several mutations by comparison with the spike protein of initial isolates. Our structural analysis revealed that only positions K417 and N501 are within the D-peptides' binding interface with the spike RBD (Figure 7). Next, we performed free-energy calculations with the Crooks Gaussian intersection (CGI) method using the dual-system single-box approximation to predict to what extent our designs will target the RBD of the most current circulating SARS-CoV-2 isolates (Figure S9). To calculate the effect of different mutations within the RBD region: K417N ($\Delta\Delta G$ = 3.80 ± 0.82 kJ/mol), K417T ($\Delta\Delta G$ = 5.34 ± 0.66 kJ/mol), E484K ($\Delta\Delta G$ = 1.28 ± 0.46 kJ/mol) and N501Y ($\Delta\Delta G$ = −11.96 ± 0.79 kJ/mol) over the D-peptides' binding affinity, we chose Covid3 (Figure 8) as a study case. The free-energy calculations indicated that mutation N501Y must increase the binding affinity of Covid3 by the RBD, while mutations K417N or K417T could have a negative effect. As expected, the mutation E484K might have a negligible effect on the Covid3-binding affinity. Overall, the combined effect of these mutations did not drop the binding affinity of Covid3 by the RBD of the new circulating variants.

Finally, we investigated the ability of Covid3 and Covid_extended_1 to inhibit the infection of Vero cells by SARS-CoV-2 variants B.1.1.7 and B.1.351. Different concentrations of both peptides were mixed with 100 $TCID_{50}$ of both variants before being incubated to Vero cells monolayers. Covid_extended_1 and Covid3 inhibited the infection of variant B.1.1.7 with IC_{50}'s of 5.57 ± 4.04 and 33.40 ± 10.75 μM, respectively. For variant B.1.351, Covid_extended_1 and Covid3 blocked the infection with IC_{50}'s of 7.37 ± 1.80 and 11.13 ± 3.82 μM, respectively (Figure 9). We also included a rabbit polyclonal antibody (40150-T62-COV2, Sino Biological Inc., Beijing, China) and the first international standard for anti-SARS-CoV-2 immunoglobulin (NIBSC code 20/136) as positive controls. The virus neutralization for controls and D-peptides as a function of the dilution ratio is shown in Figure S10. Of relevance, the K_i values estimated from the IC_{50} of the virus neutralization assays were in the same potency range as the ones obtained for the SARS-CoV-2 early lineage (Table SIII). These results confirmed that both D-peptides effectively inhibited two of the most current circulating variants.

https://doi.org/10.1021/acs.jmedchem.1c00655
J. Med. Chem. XXXX, XXX, XXX−XXX

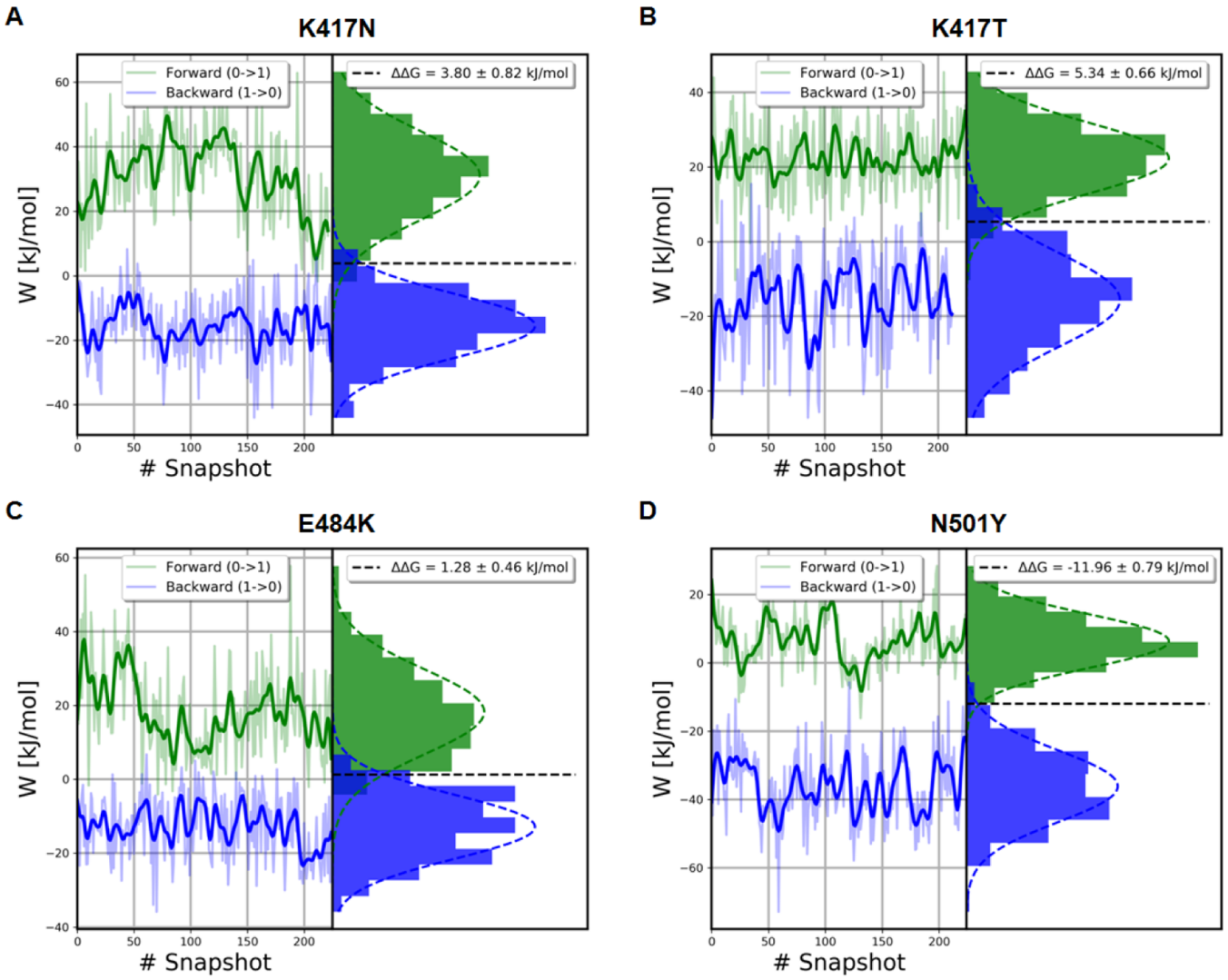

Figure 8. Predicting the effect of mutations in the SARS-CoV-2 RBD on the binding affinity of Covid3. (A) K417N, (B) K417T, (C) E484K, and (D) N501Y. Free-energy calculations were performed with the CGI method using the dual-system single-box approach.

DISCUSSION

Targeting the RBD−ACE2 interaction with linear peptides derived from the ACE2 N-terminus-binding helix is a strategy supported by previous computational and experimental studies.[31,33,34] Here, we reported the design of three D-peptides named Covid_extended_1, Covid3, and Covid4 that bind the SARS-CoV-2 RBD with an affinity of 29, 31, and 105 nM, respectively. To engineer the novel D-analogues of the ACE2-binding helix, we searched our D-PDB database for similar configurations of the critical hotspots within the N-terminus helix: Q24, T27, K31, H34, D38, and Y41 predicted by our CAS. Deep mutagenesis studies on the ACE2-binding interface supported our hotspot predictions.[34] MD simulations revealed a stable binding mode of the D-peptide analogues to the SARS-CoV2 RBD. This feature is significant considering the flat surface of the RBD-binding motif.

Covid_extended_1 and Covid3 have similar binding affinities for the RBD as the native ACE2 receptor (K_d = 8.8 ± 0.17 nM). Both peptides bind 43-fold stronger to the RBD than a 23 mer L-peptide (I21−S44, K_d = 1.3 μM) derived from the ACE2 N-terminus helix.[34] The higher content of α-helical secondary structure of the design of D-peptides in solution might explain this result. As expected, the extension of Covid4 by adding the RI sequence of the hairpin loop increases the binding affinity of the resulting peptide (Covid_extended_1), given the critical contribution of three residues (K353, D355, and R357) within this loop to the binding affinity of the RBD−ACE2 complex. Our results validate a recent computational study proposing that linking the ACE2 N-terminus α-helical peptide with the hairpin loop L351−R357 improves the hybrid peptide's binding affinity for the RBD.[33] A similar idea was explored in the past to improve the antiviral activity of ACE2-derived peptides against SARS-CoV infection.[35]

The binding of the D-peptides to the full spike should be similar to the RBD. The trimeric nature of the spike should not affect the binding process of the D-peptides (3 peptides per spike), given the overlap between the binding site of these peptides with the ACE2. Previously, the binding of miniprotein inhibitors to each protomer of the full spike through CryoEM structure determinations was described.[13] Of note, these miniproteins have three times the molecular weight of our D-peptides.

The molecular recognition of viral surface proteins by high-affinity reagents is a promising strategy for virus neutralization. Several proteins targeting the RBD−ACE2 interaction have

https://doi.org/10.1021/acs.jmedchem.1c00655
J. Med. Chem. XXXX, XXX, XXX−XXX

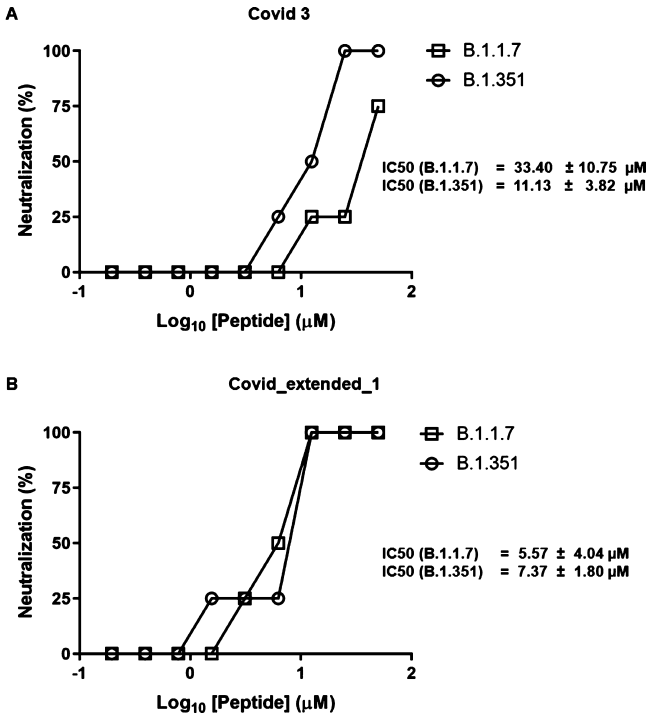

Figure 9. D-peptides neutralize the infection of Vero cells by SARS-CoV-2 variants B.1.1.7 and B.1.351. (A) Neutralization activity of Covid3. (B) Neutralization activity of Covid_extended_1. Different concentrations of both peptides were mixed with 100 $TCID_{50}$ of SARS-CoV-2 before being incubated with Vero cell monolayers. Covid3 neutralized the infection of variants B.1.1.7 and B.1.351 with IC_{50}'s of 33.40 ± 10.75 and 11.13 ± 3.82 μM, respectively. Covid_extended_1 neutralized the infection of variants B.1.1.7 and B.1.351 with IC_{50}'s of 5.57 ± 4.04 and 7.37 ± 1.80 μM, respectively.

been described. Soluble human and modified ACE2 showed a high affinity to the SARS-CoV-2 spike RBD, neutralizing activity in live virus infection models.[29,36] Also, numerous neutralizing antibodies, nanobodies, and synthetic proteins binding to the SARS-CoV-2-spike-RBD have been described.[13,27,37] Remarkably, we showed that Covid_extended_1 and Covid3 neutralized SARS-CoV-2 infection of Vero cells with an IC_{50} of 5.76 and 6.56 μM, respectively. Of relevance, both peptides neutralized with a similar potency the infection of two variants of concern: B.1.1.7 and B.1.351. Our results suggested that both peptides should also inhibit the infection of variant P1 (N501Y, K417T, and E484K) given its similar mutation pattern in the RBD with the variant B.1.351 (N501Y, K417N, and E484K).

Time addition experiments are a valuable strategy to determine which stage of the virus life cycle is targeted by different ligands. A previous report showed that LCB1, a miniprotein SARS-CoV-2 inhibitor, can effectively inhibit cell fusion by co-incubating with SARS-CoV-2 at −1 and 0 h before adding the mix to Vero cells.[38] Here, we mixed different concentrations of the D-peptides with 100 $TCID_{50}$ of the SARS-CoV-2 isolates for 30 min at 37 °C before incubating the mix with the cells. Therefore, we did not expect to see a different mechanism of action for our designs if we preincubated these peptides with the virus during a similar time range. We based this hypothesis on the fact that our designs and LCB1 target a similar region of the RBD.

There is no discrepancy between the two-digit nM binding affinity of Covid3 and Covid_extended1 and the single-digit μM IC_{50} obtained from virus neutralization assays. The potency of the peptides (K_i) estimated through the Cheng–Prusoff equation[32] are in the same potency range as the RBD + D-peptide binding affinities (K_d = 29 and 31 nM) obtained through the BLI experiments. A previous study also described a drop (35-fold) in the activity of the SARS-CoV-2 miniprotein inhibitor AHB1, which binds to the RBD with a $K_d \approx 1$ nM and neutralizes SARS-CoV-2 infection in VeroE6 cells with an IC_{50} = 35 nM.[13]

While the most potent neutralizing antibody thus far described is far more potent on a molar basis (IC_{50} = 13 nM),[22] our peptides have far lower molecular weight than an antibody, and thus, the potency on a per gram basis is much closer [Covid3/Covid_extended_1 (22×10^{-3} g/L) and Ab (1.9×10^{-3} g/L)]. D-peptides are appropriate for the formulation in a gel for nasal administration and direct distribution into the respiratory system *via* nebulization or as a dry powder due to their small size and strong resistance to protease degradation. Other authors showed that the intranasal administration of miniproteins engineered to bind strongly to the influenza hemagglutinin could give preventive and therapeutic safety in deadly influenza infection models in rodents.[39] Finally, as our peptides can be manufactured synthetically, they will be far cheaper to produce, enabling use in cost-constrained applications. We believe that D-peptides could prove a valuable modality for the treatment of such respiratory diseases.

CONCLUSIONS

In this work, we designed two D-peptide high-affinity binders of the SARS-CoV-2 RBD that neutralized the virus infection of Vero cells in the single-digit μM range. Of relevance, both D-peptides neutralized with a similar potency the infection of two variants of concern: B.1.1.7 and B.1.351. These novel blockers of early stages in the virus infection have potential advantages as therapeutics.

EXPERIMENTAL SECTION

Design Strategy of D-Peptides. The query process for each helix segment was run independently using the latest update of the D-PDB database previously generated in our group.[26] Hotspot residues at the ACE2-binding interface were identified through a CAS using the Elaspic2 webserver (http://elaspic.kimlab.org),[28] using the full-length ACE2 in complex with the RBD (6m17) as the starting structure. Structural alignments between specific atoms in each query structure and each entry at the D-PDB database were carried out using Click.[36] This program uses the molecule coordinates to align groups of atoms independent of the residue order. This feature is essential for identifying the closest matching D-peptide hotspot constellations because their sequence order and/or direction is very often different to the L-peptide query.[26] The matched (D) hotspots from both helices were aligned with their corresponding (L) hotspots. We added two (DAla–DAla) or three extra residues (DIle–DAla–DAla) to assemble both helices of each D-peptide over the surface of the spike RBD (6vw1) using Chimera (Table 1).[37]

MD Simulations. All the MD simulations of the spike + D-peptide complexes were carried out with the GROMACS software package[40] version 2019.3 using the CHARMM36-m force field[41] and the TIP3P water model.[42] The simulation systems consist of each complex solvated in an octahedron box with ∼16278 water molecules. The electroneutrality was ensured by adding sufficient Na^+Cl^- counterions to each solvation box. All the systems were relaxed through two consecutive energy minimization (EM) protocols. Then, each system was heated in the *NVT* ensemble and then equilibrated in the *NPT* ensemble at p = 1 bar and T = 310 K. In both steps, we released

https://doi.org/10.1021/acs.jmedchem.1c00655
J. Med. Chem. XXXX, XXX, XXX−XXX

gradually the position restrains that apply over the protein heavy atoms. Finally, the production *NPT* runs were conducted by duplicating for 200 ns. The EM and MD simulations were set up similarly to previous works.[43,44]

All the trajectory analyses were carried out with the GROMACS software package[40] version 2019.3. The most representative structure sampled by each complex along the MD simulations was calculated over the complex heavy atoms with the GROMOS algorithm[45] implemented in the gmx cluster program,[40] using an rmsd cutoff value of 0.15 nm.

Free-Energy Calculations Using the CGI Method. We set up free-energy calculations with the CGI protocol using the dual-system single-box approximation to predict the effect of different mutations in the RBD on the D-peptides' binding ability. Briefly, in the dual-system single-box setup, a wild-type RBD bound to a D-peptide is positioned in the same box with a solvated unbound mutant RBD ($\lambda = 0$). The other end state ($\lambda = 1$) contains a mutant RBD bound to a D-peptide with a solvated wild-type RBD (Figure S9).[46] To prevent an interaction between the solvated RBD and the RBD + peptide complex due to motions during the simulation, position restraints were applied at the backbone atoms of the RBD Val32. Simulation topologies and input files were generated for the CHARMM36-m force field[41] with the pmx package.[47] For each state ($\lambda = 0$ and $\lambda = 1$), an equilibrium MD simulations of 100 ns length were conducted using the simulation parameters described previously.[48] From each trajectory, the first 10 ns were discarded, snapshots were taken every 400 ps, and short nonequilibrium thermodynamic integration runs (500 ps) were performed in which λ was switched from 0 to 1 or from 1 to 0, respectively. The derivative of the Hamiltonian with respect to λ was recorded at every step and the alchemical free energy for the transition was calculated according to Goette and Grübmueller.[49] The free-energy estimate corresponds to a double free-energy difference: $\Delta\Delta G = \Delta G_4 - \Delta G_3$ (Figure S9).

Peptide Synthesis. All peptides were synthesized, purified, and characterized by Lifetein LLC. We described briefly the protocol provided by the supplier. The peptides were synthesized on ChemMatrix Rink Amide resin, using the standard Fmoc synthesis protocol with DIC/Cl-HOBt coupling, on an APEX 396 automatic synthesizer. The resin was swollen in DMF for 30 min, treated with 20v% piperidine−DMF for 8 min to remove the Fmoc protecting group at 50 °C, and washed with DMF three times. For the coupling reaction, the resin was added with Fmoc-protected amino acid, Cl-HOBt, DIC, and NMP. The mixture was vortexed for 20 min at 50 °C. Afterward, the resin was washed with DMF once. The cycle of deprotection and coupling steps was repeated until the last amino acid residue was assembled. After the final Fmoc-protecting group was removed, the resin was treated with 20v% acetic anhydride−NMP for 20 min. The resin was then washed with DMF and DCM and dried with air. The peptides were cleaved using a TFA cocktail (95v% TFA, 2.5v% water, and 2.5v% TIS) for 3 h. Crude peptides were precipitated by adding ice-chilled anhydrous ethyl ether, washed with anhydrous ethyl ether three times, and dried in vacuo. All peptides' purity is higher than 95%. In the Supporting Information material, we provided the details about the characterization of these peptides (weight, molecular weight, purity, HPLC, and MS) (Table SIV and Figures S11−S14).

CD Measurements. Freeze-dried peptides as supplied by LifeTein were resuspended in 1:4 acetonitrile/phosphate-buffered saline (PBS) to solubilize them at concentrations required for CD.[50] Measurements were recorded in a JASCO J-1500 CD spectrophotometer at the Structural and Biophysical Core Facility—The Hospital for Sick Children, Toronto, Canada. Spectra were collected from 190 to 260 nm, with a data pitch of 1 nm, an integration time of 2 s, and a scanning speed of 50 nm/min. The data presented are the result of three averaged measurements for every peptide. Peptides were prepared aiming at a concentration of 10 μM per sample, but the absolute concentration was calculated by amino acid analysis performed by the SPARC BioCentre—The Hospital for Sick Children, Toronto, Canada.

A baseline measurement of 1:4 acetonitrile/PBS was recorded and subtracted from the peptide spectra. The baseline-subtracted data in millidegree units were converted to the standard molar ellipticity units (degrees cm^2 dmol^{-1}) to normalize the data by peptide amount. The spectra were plotted in GraphPad PRISM 9.

SEC Purification. All peptides were resuspended in PBS containing 10% ACN to a final concentration of 1 μM. Gel filtration was performed in a Superdex 75 10/300 GL pre-equilibrated in PBS, 10% ACN. The column was connected to an AKTA Pure 25 system. For each peptide, 500 μL aliquots at 1 μM were loaded and further eluted by isocratic elution at 0.5 mL/min. All data were plotted in PRISM 9 for ease of presentation.

D-Peptide BLI Measurements. BLI measurements were performed with ForteBio Octet RED96 instrument and ForteBio biosensors. Data analyses used ForteBio Data Analysis 9.0 software. Kinetics assays were carried out at 25 °C using settings of the standard kinetic acquisition rate (5.0 Hz, averaging by 20) at a sample plate shake speed of 1000 rpm.

His-tagged RBD purified protein was loaded onto Ni-NTA sensors at a concentration of 200 nM. Peptides were loaded at different concentrations to the bound sensors. The dissociation step was monitored by dipping bound sensors back into the wells used to collect the baseline time course. To subtract binding due to nonspecific interactions of the peptides with the sensors, nonspecific His-tagged SUMO protein and His-tagged RBD loaded alone were used as controls. The subtracted binding curves were analyzed to obtain association rate constant k_a, k_d, and K_d values.

Protease Stability Assays. Stocks of 20 μM peptide in 200 μL of total volume (10 mM Tris-base, 10 mM NaCl, pH 7.4) were supplemented with 5 μM $CaCl_2$, and 30 μL was removed for the untreated T0 sample. ProtK (Bioshop) was then added to a final concentration of 100 μg/mL. Samples were incubated at 37 °C, and 30 μL was removed after each time point and protease activity was blocked by the addition of 10 mM PMSF (200 mM stock dissolved in isopropanol). Protease-inactivated samples were frozen at−20 °C until further use. Digestions were repeated three times. Frozen samples were supplemented with 8 μL of sample loading buffer (4× NuPAGE; Thermo Fisher Scientific), boiled (50 °C) for 10 min, and centrifuged (16,128*g*, 10 min) before loading the gel [12% NuPAGE Bis-Tris (ThermoFisher Scientific)] with Mes running buffer. Gels were run at 200 V for ∼35 min and stained using Coomassie Brilliant Blue dye. Densitometry of bands was determined using ImageJ software with background subtraction. All samples were normalized to the irrespective untreated sample (T0).

Virus Neutralization Assays. The SARS-CoV-2 (βCoV/Korea/KCDC/2020 NCCP43326), SARS-CoV-2 B.1.1.7 (hCoV-19/Korea/KDCA51463/2021), and SARS-CoV-2 B.1.351 (hCoV-19/Korea/KDCA55905/2021) isolates were obtained from the Korea Disease Control and Prevention Agency. These lineages were propagated in Vero cells (ATCC CCL-81) in Dulbecco's modified Eagle's medium (DMEM, Welgene, Gyeongsan, Republic of Korea) in the presence of 2% fetal bovine serum (Gibco, Thermo Scientific, Waltham, MA, USA). The cells were grown in T-75 flasks, inoculated with SARS-CoV-2, and incubated at 37 °C in a 5% CO_2 environment. Three days after inoculation, the viruses were harvested and stored at −80 °C. The virus titer was determined by a $TCID_{50}$ assay (Table SV).[51]

The neutralization assay was performed as previously described.[52,53] Briefly, Vero cells were seeded in 96-well plates (1.5×10^4 cells/well) in Opti-PRO SFM (Thermo Scientific, Waltham, MA, USA) supplemented with 4 mM L-glutamine and 1× Antibiotics-Antimycotic (Thermo Scientific, Waltham, MA, USA) and grown for 24 h at 37 °C in a 5% CO_2 environment. Peptides were dissolved in 100% dimethyl sulfoxide (DMSO, Sigma-Aldrich, St. Louis, MO, USA) and diluted in PBS (Welgene, Gyeongsan, Republic of Korea) from the maximum concentration of 100 μM to the lowest concentration of 0.1953 μM. Twofold serially diluted peptides were mixed with 100 $TCID_{50}$ of SARS-CoV-2, and the mixture was incubated for 30 min at 37 °C. Then, the mixture was added to the Vero cells in tetrad and incubated for 4 days at 37 °C in a 5% CO_2 environment. The cytopathic effect in each well was visualized

https://doi.org/10.1021/acs.jmedchem.1c00655
J. Med. Chem. XXXX, XXX, XXX−XXX

following crystal violet staining 4 days post-infection. The IC_{50} values were calculated using the dose−response inhibition equation of GraphPad Prism 6 (GraphPad Software, La Jolla, CA, USA). To determine the cell toxicity, similar experiments were performed without the addition of the virus. Cell viability was measured using MTS solution. We included the following as a positive control of the virus neutralization experiments: (i) a rabbit polyclonal antibody (40150-T62-COV2, Sino Biological Inc., Beijing, China) and (ii) the first international standard for anti-SARS-CoV-2 immunoglobulin (NIBSC code 20/136). As a negative control, we used PBS (data not shown). We also plotted the % of virus neutralization as a function of the dilution ratio for all the controls and the D-peptides in the Supporting Information material (Figures S7 and S10).

Finally, we used the Cheng−Prusoff equation[32] to estimate the K_i of the designed peptides from the IC_{50} values obtained in the virus neutralization assays. In this case, we adapted the equation used to calculate the constant inhibition at cellular receptors to virus neutralization assays (1)

$$K_i = \frac{IC_{50}}{[A]/TCID_{50}+1} \quad (1)$$

where $[A]$ is the fixed infective dose of SARS-CoV2 used in the virus neutralization assays ($[A]$ = 100 $TCID_{50}$) and $TCID_{50}$ is the fifty-percent tissue-culture-infective dose.

■ ASSOCIATED CONTENT

Supporting Information

The Supporting Information is available free of charge at https://pubs.acs.org/doi/10.1021/acs.jmedchem.1c00655.

Identification of the hotspot residues of the ACE2 receptor for binding the SARS-CoV-2 spike RBD; rmsd distribution profiles of the D-PDB database to identify D-peptide analogues of helix1 and helix2; glycosylation sites at positions N331 and N343 are too far from the D-peptide-binding site in the RBD; RMSF of the heavy atoms of the design of D-peptides bound to the RBD; assessment of the binding mode stability of the 3D structure of the RBD + D-peptide complexes: structural superposition of the initial [receptor (light blue) and Covid3 (salmon)] and final [receptor (dark blue) and Covid3 (red)] structures of the RBD + Covid3 complex and structural superposition of the initial [receptor (light blue) and Covid4 (salmon)] and final [receptor (dark blue) and Covid4 (red)] structures of the RBD + Covid4 complex; SEC of the D-peptides Covid3, Covid_extended_1, and Covid4, for each spectrum, the red line indicated the conductance and the blue line the UV absorbance at 280 nm; virus neutralization for controls and D-peptides as a function of the dilution ratio: Covid3, Covid extended 1, SARS-CoV-2 Neut Ab (40150-T62-COV2), and International standard for anti-SARS-CoV-2 antibody (NIBSC code 20/136); cell viability after incubating Vero cells with different concentrations of the design of D-peptides: Covid 3 and Covid_extended_1; free-energy calculations using the dual-system single-box setup: thermodynamic cycle and system setup $\Delta\Delta G = \Delta G_4 - \Delta G_3$; virus neutralization (B.1.1.7 and B.1.351) for controls and D-peptides as a function of the dilution ratio: Covid3, Covid extended 1, SARS-CoV-2 Neut Ab (40150-T62-COV2), and International standard for anti-SARS-CoV-2 antibody (NIBSC code 20/136) for SARS-CoV-2 B.1.1.7 variant, Covid3, Covid extended 1, SARS-CoV-2 Neut Ab (40150-T62-COV2), and International Standard for anti-SARS-CoV-2 antibody (NIBSC code 20/136), for SARS-CoV-2 B.1.351 variant; HPLC report of the D-peptide Covid3; mass spectrometry report of the D-peptide Covid3; HPLC report of the D-peptide Covid_extended_1; mass spectrometry report of the D-peptide Covid_extended_1; different sets of atom levels defined for each hotspot; D-matches obtained for helix1 and helix2 to build the design of D-peptides; conversion of IC_{50} values obtained in the virus neutralization assays to K_i; certificate of analysis of the design of D-peptides; and titers and $TCID_{50}$ of the different SARS-CoV-2 variants (PDF)

RBD + Covid3 complex (PDB)

RBD + Covid4 complex (PDB)

■ AUTHOR INFORMATION

Corresponding Author

Philip M. Kim − *Donnelly Centre for Cellular and Biomolecular Research, University of Toronto, Toronto, Ontario M5S 3E1, Canada; Department of Molecular Genetics and Department of Computer Science, University of Toronto, Toronto, Ontario M5S 3E1, Canada*; Email: pm.kim@utoronto.ca

Authors

Pedro A. Valiente − *Donnelly Centre for Cellular and Biomolecular Research, University of Toronto, Toronto, Ontario M5S 3E1, Canada*; orcid.org/0000-0002-4776-6017

Han Wen − *Donnelly Centre for Cellular and Biomolecular Research, University of Toronto, Toronto, Ontario M5S 3E1, Canada*

Satra Nim − *Donnelly Centre for Cellular and Biomolecular Research, University of Toronto, Toronto, Ontario M5S 3E1, Canada*

JinAh Lee − *Zoonotic Virus Laboratory, Institut Pasteur Korea, Seongnam-si, Gyeonggi-do 13488, Republic of Korea*

Hyeon Ju Kim − *Zoonotic Virus Laboratory, Institut Pasteur Korea, Seongnam-si, Gyeonggi-do 13488, Republic of Korea*

Jinhee Kim − *Zoonotic Virus Laboratory, Institut Pasteur Korea, Seongnam-si, Gyeonggi-do 13488, Republic of Korea*

Albert Perez-Riba − *Donnelly Centre for Cellular and Biomolecular Research, University of Toronto, Toronto, Ontario M5S 3E1, Canada*

Yagya Prasad Paudel − *Donnelly Centre for Cellular and Biomolecular Research, University of Toronto, Toronto, Ontario M5S 3E1, Canada*

Insu Hwang − *Center for Convergent Research of Emerging Virus Infection, Korea Research Institute of Chemical Technology, Daejeon 34114, Republic of Korea*

Kyun-Do Kim − *Center for Convergent Research of Emerging Virus Infection, Korea Research Institute of Chemical Technology, Daejeon 34114, Republic of Korea*

Seungtaek Kim − *Zoonotic Virus Laboratory, Institut Pasteur Korea, Seongnam-si, Gyeonggi-do 13488, Republic of Korea*

Complete contact information is available at: https://pubs.acs.org/10.1021/acs.jmedchem.1c00655

Author Contributions

P.A.V. and H.W. contributed equally. P.A.V., H.W., and P.M.K. conceptualized the study. D-peptide design and molecular dynamics simulations were carried out by P.A.V. and H.W.

https://doi.org/10.1021/acs.jmedchem.1c00655
J. Med. Chem. XXXX, XXX, XXX−XXX

Biolayer interferometry and proteinase K degradation experiments were carried out by S.N. Circular dichroism measurements were performed by A.P.R. Size-exclusion chromatography analyses were performed by A.P.R. and Y.Y.P. J.L., H.J.K., I.H., J.K., K.-D.K., and S.K. performed virus neutralization and cellular viability assays. P.A.V, S.N., and P.M.K. wrote the manuscript with input from all other authors. P.M.K. led and supervised research.

Notes

The authors declare no competing financial interest.

■ ACKNOWLEDGMENTS

P.M.K. acknowledges funding from Project Grants #PJT-166008 and #PJT-153279 from the Canadian Institute for Health Research. S.N. acknowledges Greg Wasney from the Structural & Biophysical Core (SBC) Facility, Peter Gilgan Centre for Research & Learning &The Hospital for Sick Children for his support in the BLI experiments. S.K. acknowledges funding from Project Grant #NRF-2017M3A9G6068245 from the National Research Foundation of Korea (NRF). KK acknowledges the National Research Council of Science and Technology (NST) grant through the Korean government (MSIP) (CRC-16-01-KRICT). The pathogen resources (NCCP43326, NCCP43381, and NCCP43382) for this study were provided by the National Culture Collection for Pathogens. We thank Resolute Bio Inc. for support for the synthesis of one of the peptides, and thank Bradley L. Pentelute, Tomi Sawyer, Allison Shrier, and Stephen Kennedy Smith for insightful discussions.

■ ABBREVIATIONS

ACE, acetyl group; ACE2, angiotensin-converting enzyme 2; BLI, biolayer interferometry; CAS, computational alanine scanning; CD, circular dichroism; CGI, Crooks Gaussian intersection; Cl-HOBt, 6-chloro-1-hydroxybenzotriazole; DCM, dichloromethane; DIC, diisopropylcarbodiimide; DMEM, Dulbecco's modified Eagle's medium; DMF, *N*,*N*-dimethylmethanamide; DMSO, dimethyl sulfoxide; EM, energy minimization; Fmoc, 9-fluorenylmethyl; His-tagged, histidine tag; HPLC, high-pressure liquid chromatography; IC_{50}, half maximal inhibitory concentration; k_a, association rate constant; k_d, dissociation rate constant; K_d, dissociation constant; MD, molecular dynamics; MERS-CoV, Middle East respiratory syndrome coronavirus; MS, mass spectra; Ni-NTA, nitrilotriacetic acid; NH_2, amide group; NMP, *N*-methyl-2-pyrrolidone; PBS, phosphate-buffered saline; PDB, protein data bank; ProtK, proteinase K; RBD, receptor-binding domain; RI, retro-inverse; rmsd, root-mean-square deviation; RMSF, root-mean-square fluctuation; SARS-CoV, severe acute respiratory syndrome coronavirus; SARS-CoV-2, severe acute respiratory syndrome coronavirus 2; $TCID_{50}$, fifty-percent tissue-culture-infective dose; TFA, trifluoroacetic acid

■ REFERENCES

(1) Wang, C.; Horby, P. W.; Hayden, F. G.; Gao, G. F. A novel coronavirus outbreak of global health concern. *Lancet* **2020**, *395*, 470−473.

(2) Li, F. Structure, function, and evolution of coronavirus spike proteins. *Annu. Rev. Virol.* **2016**, *3*, 237−261.

(3) Simmons, G.; Zmora, P.; Gierer, S.; Heurich, A.; Pöhlmann, S. Proteolytic activation of the SARS-coronavirus spike protein: cutting enzymes at the cutting edge of antiviral research. *Antivir. Res.* **2013**, *100*, 605−614.

(4) Matsuyama, S.; Nagata, N.; Shirato, K.; Kawase, M.; Takeda, M.; Taguchi, F. Efficient activation of the severe acute respiratory syndrome coronavirus spike protein by the transmembrane protease TMPRSS2. *J. Virol.* **2010**, *84*, 12658−12664.

(5) Bertram, S.; Glowacka, I.; Müller, M. A.; Lavender, H.; Gnirss, K.; Nehlmeier, I.; Niemeyer, D.; He, Y.; Simmons, G.; Drosten, C.; Soilleux, E. J.; Jahn, O.; Steffen, I.; Pöhlmann, S. Cleavage and activation of the severe acute respiratory syndrome coronavirus spike protein by human airway trypsin-like protease. *J. Virol.* **2011**, *85*, 13363−13372.

(6) Belouzard, S.; Chu, V. C.; Whittaker, G. R. Activation of the SARS coronavirus spike protein via sequential proteolytic cleavage at two distinct sites. *Proc. Natl. Acad. Sci. U.S.A.* **2009**, *106*, 5871−5876.

(7) Zhou, P.; Yang, X.-L.; Wang, X.-G.; Hu, B.; Zhang, L.; Zhang, W.; Si, H.-R.; Zhu, Y.; Li, B.; Huang, C.-L.; Chen, H.-D.; Chen, J.; Luo, Y.; Guo, H.; Jiang, R.-D.; Liu, M.-Q.; Chen, Y.; Shen, X.-R.; Wang, X.; Zheng, X.-S.; Zhao, K.; Chen, Q.-J.; Deng, F.; Liu, L.-L.; Yan, B.; Zhan, F.-X.; Wang, Y.-Y.; Xiao, G.-F.; Shi, Z.-L. A pneumonia outbreak associated with a new coronavirus of probable bat origin. *Nature* **2020**, *579*, 270−273.

(8) Walls, A. C.; Park, Y.-J.; Tortorici, M. A.; Wall, A.; McGuire, A. T.; Veesler, D. Structure, Function, and Antigenicity of the SARS-CoV-2 Spike Glycoprotein. *Cell* **2020**, *181*, 281−292.

(9) Hoffmann, M.; Kleine-Weber, H.; Schroeder, S.; Krüger, N.; Herrler, T.; Erichsen, S.; Schiergens, T. S.; Herrler, G.; Wu, N.-H.; Nitsche, A.; Müller, M. A.; Drosten, C.; Pöhlmann, S. SARS-CoV-2 Cell Entry Depends on ACE2 and TMPRSS2 and Is Blocked by a Clinically Proven Protease Inhibitor. *Cell* **2020**, *181*, 271−280.

(10) Wang, Q.; Zhang, Y.; Wu, L.; Niu, S.; Song, C.; Zhang, Z.; Lu, G.; Qiao, C.; Hu, Y.; Yuen, K.-Y.; Wang, Q.; Zhou, H.; Yan, J.; Qi, J. Structural and Functional Basis of SARS-CoV-2 Entry by Using Human ACE2. *Cell* **2020**, *181*, 894−904.

(11) Wrapp, D.; Wang, N.; Corbett, K. S.; Goldsmith, J. A.; Hsieh, C.-L.; Abiona, O.; Graham, B. S.; McLellan, J. S. Cryo-EM structure of the 2019-nCoV spike in the prefusion conformation. *Science* **2020**, *367*, 1260−1263.

(12) Hou, Y. J.; Okuda, K.; Edwards, C. E.; Martinez, D. R.; Asakura, T.; Dinnon, K. H., 3rd; Kato, T.; Lee, R. E.; Yount, B. L.; Mascenik, T. M.; Chen, G.; Olivier, K. N.; Ghio, A.; Tse, L. V.; Leist, S. R.; Gralinski, L. E.; Schäfer, A.; Dang, H.; Gilmore, R.; Nakano, S.; Sun, L.; Fulcher, M. L.; Livraghi-Butrico, A.; Nicely, N. I.; Cameron, M.; Cameron, C.; Kelvin, D. J.; de Silva, A.; Margolis, D. M.; Markmann, A.; Bartelt, L.; Zumwalt, R.; Martinez, F. J.; Salvatore, S. P.; Borczuk, A.; Tata, P. R.; Sontake, V.; Kimple, A.; Jaspers, I.; O'Neal, W. K.; Randell, S. H.; Boucher, R. C.; Baric, R. S. SARS-CoV-2 Reverse Genetics Reveals a Variable Infection Gradient in the Respiratory Tract. *Cell* **2020**, *182*, 429−446.

(13) Cao, L.; Goreshnik, I.; Coventry, B.; Case, J. B.; Miller, L.; Kozodoy, L.; Chen, R. E.; Carter, L.; Walls, A. C.; Park, Y.-J.; Strauch, E.-M.; Stewart, L.; Diamond, M. S.; Veesler, D.; Baker, D. De novo design of picomolar SARS-CoV-2 miniprotein inhibitors. *Science* **2020**, *370*, 426−431.

(14) Byrnes, J. R.; Zhou, X. X.; Lui, I.; Elledge, S. K.; Glasgow, J. E.; Lim, S. A.; Loudermilk, R. P.; Chiu, C. Y.; Wang, T. T.; Wilson, M. R.; Leung, K. K.; Wells, J. A. Competitive SARS-CoV-2 Serology Reveals Most Antibodies Targeting the Spike Receptor-Binding Domain Compete for ACE2 Binding. *mSphere* **2020**, *5*, No. e00802.

(15) Shi, R.; Shan, C.; Duan, X.; Chen, Z.; Liu, P.; Song, J.; Song, T.; Bi, X.; Han, C.; Wu, L.; Gao, G.; Hu, X.; Zhang, Y.; Tong, Z.; Huang, W.; Liu, W. J.; Wu, G.; Zhang, B.; Wang, L.; Qi, J.; Feng, H.; Wang, F.-S.; Wang, Q.; Gao, G. F.; Yuan, Z.; Yan, J. A human neutralizing antibody targets the receptor-binding site of SARS-CoV-2. *Nature* **2020**, *584*, 120−124.

(16) Ju, B.; Zhang, Q.; Ge, J.; Wang, R.; Sun, J.; Ge, X.; Yu, J.; Shan, S.; Zhou, B.; Song, S.; Tang, X.; Yu, J.; Lan, J.; Yuan, J.; Wang, H.; Zhao, J.; Zhang, S.; Wang, Y.; Shi, X.; Liu, L.; Zhao, J.; Wang, X.; Zhang, Z.; Zhang, L. Human neutralizing antibodies elicited by SARS-CoV-2 infection. *Nature* **2020**, *584*, 115−119.

https://doi.org/10.1021/acs.jmedchem.1c00655
J. Med. Chem. XXXX, XXX, XXX−XXX

(17) Wang, C.; Li, W.; Drabek, D.; Okba, N. M. A.; van Haperen, R.; Osterhaus, A. D. M. E.; van Kuppeveld, F. J. M.; Haagmans, B. L.; Grosveld, F.; Bosch, B.-J. A human monoclonal antibody blocking SARS-CoV-2 infection. *Nat. Commun.* **2020**, *11*, 2251.
(18) Yuan, M.; Wu, N. C.; Zhu, X.; Lee, C.-C. D.; So, R. T. Y.; Lv, H.; Mok, C. K. P.; Wilson, I. A. A highly conserved cryptic epitope in the receptor binding domains of SARS-CoV-2 and SARS-CoV. *Science* **2020**, *368*, 630−633.
(19) Zhou, D.; Duyvesteyn, H. M. E.; Chen, C.-P.; Huang, C.-G.; Chen, T.-H.; Shih, S.-R.; Lin, Y.-C.; Cheng, C.-Y.; Cheng, S.-H.; Huang, Y.-C.; Lin, T.-Y.; Ma, C.; Huo, J.; Carrique, L.; Malinauskas, T.; Ruza, R. R.; Shah, P. N. M.; Tan, T. K.; Rijal, P.; Donat, R. F.; Godwin, K.; Buttigieg, K. R.; Tree, J. A.; Radecke, J.; Paterson, N. G.; Supasa, P.; Mongkolsapaya, J.; Screaton, G. R.; Carroll, M. W.; Gilbert-Jaramillo, J.; Knight, M. L.; James, W.; Owens, R. J.; Naismith, J. H.; Townsend, A. R.; Fry, E. E.; Zhao, Y.; Ren, J.; Stuart, D. I.; Huang, K.-Y. A. Structural basis for the neutralization of SARS-CoV-2 by an antibody from a convalescent patient. *Nat. Struct. Mol. Biol.* **2020**, *27*, 950−958.
(20) Liu, L.; Wang, P.; Nair, M. S.; Yu, J.; Rapp, M.; Wang, Q.; Luo, Y.; Chan, J. F.-W.; Sahi, V.; Figueroa, A.; Guo, X. V.; Cerutti, G.; Bimela, J.; Gorman, J.; Zhou, T.; Chen, Z.; Yuen, K.-Y.; Kwong, P. D.; Sodroski, J. G.; Yin, M. T.; Sheng, Z.; Huang, Y.; Shapiro, L.; Ho, D. D. Potent neutralizing antibodies against multiple epitopes on SARS-CoV-2 spike. *Nature* **2020**, *584*, 450−456.
(21) Zost, S. J.; Gilchuk, P.; Case, J. B.; Binshtein, E.; Chen, R. E.; Nkolola, J. P.; Schäfer, A.; Reidy, J. X.; Trivette, A.; Nargi, R. S.; Sutton, R. E.; Suryadevara, N.; Martinez, D. R.; Williamson, L. E.; Chen, E. C.; Jones, T.; Day, S.; Myers, L.; Hassan, A. O.; Kafai, N. M.; Winkler, E. S.; Fox, J. M.; Shrihari, S.; Mueller, B. K.; Meiler, J.; Chandrashekar, A.; Mercado, N. B.; Steinhardt, J. J.; Ren, K.; Loo, Y.-M.; Kallewaard, N. L.; McCune, B. T.; Keeler, S. P.; Holtzman, M. J.; Barouch, D. H.; Gralinski, L. E.; Baric, R. S.; Thackray, L. B.; Diamond, M. S.; Carnahan, R. H.; Crowe, J. E., Jr. Potently neutralizing and protective human antibodies against SARS-CoV-2. *Nature* **2020**, *584*, 443−449.
(22) Forni, G.; Mantovani, A.; Mantovani, A.; Mantovani, A.; Moretta, L.; Rappuoli, R.; Rezza, G.; Bagnasco, A.; Barsacchi, G.; Bussolati, G.; Cacciari, M.; Cappuccinelli, P.; Cheli, E.; Guarini, R.; Bacci, M. L.; Mancini, M.; Marcuzzo, C.; Morrone, M. C.; Parisi, G.; Pasquino, G.; Patrono, C.; Curzio, A. Q.; Remuzzi, G.; Roncaglia, A.; Schiaffino, S.; Vineis, P.; on behalf of the Covid-19 Commission of Accademia Nazionale dei Lincei, R. COVID-19 vaccines: where we stand and challenges ahead. *Cell Death Differ.* **2021**, *28*, 626−639.
(23) https://www.nytimes.com/interactive/2020/science/coronavirus-vaccine-tracker.html (accessed 27-08-2021).
(24) Liu, S.; Lu, H.; Niu, J.; Xu, Y.; Wu, S.; Jiang, S. Different from the HIV fusion inhibitor C34, the anti-HIV drug Fuzeon (T-20) inhibits HIV-1 entry by targeting multiple sites in gp41 and gp120. *J. Biol. Chem.* **2005**, *280*, 11259−11273.
(25) Nishimura, Y.; Francis, J. N.; Donau, O. K.; Jesteadt, E.; Sadjadpour, R.; Smith, A. R.; Seaman, M. S.; Welch, B. D.; Martin, M. A.; Kay, M. S. Prevention and treatment of SHIVAD8 infection in rhesus macaques by a potent d-peptide HIV entry inhibitor. *Proc. Natl. Acad. Sci. U.S.A.* **2020**, *117*, 22436−22442.
(26) Garton, M.; Nim, S.; Stone, T. A.; Wang, K. E.; Deber, C. M.; Kim, P. M. Method to generate highly stable D-amino acid analogs of bioactive helical peptides using a mirror image of the entire PDB. *Proc. Natl. Acad. Sci. U.S.A.* **2018**, *115*, 1505−1510.
(27) Mulligan, M. J.; Lyke, K. E.; Kitchin, N.; Absalon, J.; Gurtman, A.; Lockhart, S.; Neuzil, K.; Raabe, V.; Bailey, R.; Swanson, K. A.; Li, P.; Koury, K.; Kalina, W.; Cooper, D.; Fontes-Garfias, C.; Shi, P.-Y.; Türeci, Ö.; Tompkins, K. R.; Walsh, E. E.; Frenck, R.; Falsey, A. R.; Dormitzer, P. R.; Gruber, W. C.; Şahin, U.; Jansen, K. U. Phase I/II study of COVID-19 RNA vaccine BNT162b1 in adults. *Nature* **2020**, *586*, 589−593.
(28) Marchetti, A.; Di Lorito, A.; Buttitta, F. Why anti-PD1/PDL1 therapy is so effective? Another piece in the puzzle. *J. Thorac. Dis.* **2017**, *9*, 4863−4866.
(29) Research, D. E. S. *Molecular Dynamics Simulations Related to SARS-CoV-2*; D. E. Shaw Research Technical Data, 2020.
(30) Casalino, L.; Gaieb, Z.; Goldsmith, J. A.; Hjorth, C. K.; Dommer, A. C.; Harbison, A. M.; Fogarty, C. A.; Barros, E. P.; Taylor, B. C.; McLellan, J. S.; Fadda, E.; Amaro, R. E. Beyond Shielding: The Roles of Glycans in the SARS-CoV-2 Spike Protein. *ACS Cent. Sci.* **2020**, *6*, 1722−1734.
(31) Huang, X.; Pearce, R.; Zhang, Y. De novo design of protein peptides to block association of the SARS-CoV-2 spike protein with human ACE2. *Aging* **2020**, *12*, 11263−11276.
(32) Cheng, Y.; Prusoff, W. H. Relationship between the inhibition constant (K1) and the concentration of inhibitor which causes 50 per cent inhibition (I50) of an enzymatic reaction. *Biochem. Pharmacol.* **1973**, *22*, 3099.
(33) Han, Y.; Král, P. Computational Design of ACE2-Based Peptide Inhibitors of SARS-CoV-2. *ACS Nano* **2020**, *14*, 5143−5147.
(34) Chan, K. K.; Dorosky, D.; Sharma, P.; Abbasi, S. A.; Dye, J. M.; Kranz, D. M.; Herbert, A. S.; Procko, E. Engineering human ACE2 to optimize binding to the spike protein of SARS coronavirus 2. *Science* **2020**, *369*, 1261−1265.
(35) Han, D. P.; Penn-Nicholson, A.; Cho, M. W. Identification of critical determinants on ACE2 for SARS-CoV entry and development of a potent entry inhibitor. *Virology* **2006**, *350*, 15−25.
(36) Nguyen, M. N.; Tan, K. P.; Madhusudhan, M. S. CLICK–topology-independent comparison of biomolecular 3D structures. *Nucleic Acids Res.* **2011**, *39*, W24−W28.
(37) Pettersen, E. F.; Goddard, T. D.; Huang, C. C.; Couch, G. S.; Greenblatt, D. M.; Meng, E. C.; Ferrin, T. E. UCSF Chimera–a visualization system for exploratory research and analysis. *J. Comput. Chem.* **2004**, *25*, 1605−1612.
(38) Zhao, M.; Su, P.-Y.; Castro, D. A.; Tripler, T. N.; Hu, Y.; Cook, M.; Ko, A. I.; Farhadian, S. F.; Israelow, B.; Dela Cruz, C. S.; Xiong, Y.; Sutton, R. E. Rapid, reliable, and reproducible cell fusion assay to quantify SARS-Cov-2 spike interaction with hACE2. *PLoS Pathog.* **2021**, *17*, No. e1009683.
(39) Chevalier, A.; Silva, D.-A.; Rocklin, G. J.; Hicks, D. R.; Vergara, R.; Murapa, P.; Bernard, S. M.; Zhang, L.; Lam, K.-H.; Yao, G.; Bahl, C. D.; Miyashita, S.-I.; Goreshnik, I.; Fuller, J. T.; Koday, M. T.; Jenkins, C. M.; Colvin, T.; Carter, L.; Bohn, A.; Bryan, C. M.; Fernández-Velasco, D. A.; Stewart, L.; Dong, M.; Huang, X.; Jin, R.; Wilson, I. A.; Fuller, D. H.; Baker, D. Massively parallel de novo protein design for targeted therapeutics. *Nature* **2017**, *550*, 74−79.
(40) Abraham, M. J.; Murtola, T.; Schulz, R.; Páll, S.; Smith, J. C.; Hess, B.; Lindahl, E. GROMACS: High performance molecular simulations through multi-level parallelism from laptops to supercomputers. *SoftwareX* **2015**, *1*−*2*, 19−25.
(41) Huang, J.; Rauscher, S.; Nawrocki, G.; Ran, T.; Feig, M.; de Groot, B. L.; Grubmüller, H.; MacKerell, A. D. CHARMM36m: an improved force field for folded and intrinsically disordered proteins. *Nat. Methods* **2017**, *14*, 71−73.
(42) Jorgensen, W. L.; Chandrasekhar, J.; Madura, J. D.; Impey, R. W.; Klein, M. L. Comparison of simple potential functions for simulating liquid water. *J. Chem. Phys.* **1983**, *79*, 926−935.
(43) Valiente, P. A.; Becerra, D.; Kim, P. M. A Method to Calculate the Relative Binding Free Energy Differences of α-Helical Stapled Peptides. *J. Org. Chem.* **2020**, *85*, 1644−1651.
(44) Mesa-Galloso, H.; Delgado-Magnero, K. H.; Cabezas, S.; López-Castilla, A.; Hernández-González, J. E.; Pedrera, L.; Alvarez, C.; Peter Tieleman, D.; García-Sáez, A. J.; Lanio, M. E.; Ros, U.; Valiente, P. A. Disrupting a key hydrophobic pair in the oligomerization interface of the actinoporins impairs their pore-forming activity. *Protein Sci.* **2017**, *26*, 550−565.
(45) Daura, X.; Gademann, K.; Jaun, B.; Seebach, D.; van Gunsteren, W. F.; Mark, A. E. Peptide Folding: When Simulation Meets Experiment. *Angew. Chem., Int. Ed.* **1999**, *38*, 236−240.
(46) Gapsys, V.; Michielssens, S.; Peters, J. H.; de Groot, B. L.; Leonov, H., Calculation of Binding Free Energies. In *Molecular Modeling of Proteins*; Kukol, A., Ed.; Springer New York: New York, NY, 2015; pp 173−209.

https://doi.org/10.1021/acs.jmedchem.1c00655
J. Med. Chem. XXXX, XXX, XXX−XXX

(47) Gapsys, V.; Michielssens, S.; Seeliger, D.; de Groot, B. L. pmx: Automated protein structure and topology generation for alchemical perturbations. *J. Comput. Chem.* **2015**, *36*, 348−354.
(48) Seeliger, D.; de Groot, B. L. Protein thermostability calculations using alchemical free energy simulations. *Biophys. J.* **2010**, *98*, 2309−2316.
(49) Goette, M.; Grubmüller, H. Accuracy and convergence of free energy differences calculated from nonequilibrium switching processes. *J. Comput. Chem.* **2009**, *30*, 447−456.
(50) Miles, J. A.; Yeo, D. J.; Rowell, P.; Rodriguez-Marin, S.; Pask, C. M.; Warriner, S. L.; Edwards, T. A.; Wilson, A. J. Hydrocarbon constrained peptides − understanding preorganisation and binding affinity. *Chem. Sci.* **2016**, *7*, 3694−3702.
(51) Reed, L. J.; Muench, H. A Simple Method Of Estimating Fifty Per Cent Endpoints12. *Am. J. Epidemiol.* **1938**, *27*, 493−497.
(52) Jiang, L.; Wang, N.; Zuo, T.; Shi, X.; Poon, K.-M. V.; Wu, Y.; Gao, F.; Li, D.; Wang, R.; Guo, J.; Fu, L.; Yuen, K.-Y.; Zheng, B.-J.; Wang, X.; Zhang, L. Potent Neutralization of MERS-CoV by Human Neutralizing Monoclonal Antibodies to the Viral Spike Glycoprotein. *Sci. Transl. Med.* **2014**, *6*, 234ra59.
(53) Kim, S. I.; Kim, S.; Kim, J.; Chang, S. Y.; Shim, J. M.; Jin, J.; Lim, C.; Baek, S.; Min, J.-Y.; Park, W. B.; Oh, M.-d.; Kim, S.; Chung, J. Generation of a Nebulizable CDR-Modified MERS-CoV Neutralizing Human Antibody. *Int. J. Mol. Sci.* **2019**, *20*, 5073.

https://doi.org/10.1021/acs.jmedchem.1c00655
J. Med. Chem. XXXX, XXX, XXX−XXX